A Contact-Model-Guided Visuotactile Sensor Enabling Simultaneous Measurement of Hardness and Tactile Information

Xiangyu Mi, Ke Qiu, Pingyu Xiang, *Graduate Student Member, IEEE*, Shudong Wang, *Member, IEEE*, Rong Xiong, *Senior Member, IEEE*, Yue Wang, *Senior Member, IEEE*, Xiazhen Yu, and Haojian Lu, *Member, IEEE*

***Abstract*—Haptics plays a crucial role in enabling robots to achieve safe and coordinated interactions with their surroundings. Among the diverse range of tactile sensors, visuotactile sensors have emerged as leading candidates for sophisticated fingertip sensing applications due to their high resolution and capability to perceive multimodal tactile information. However, current visuotactile sensors face limitations in durability and the ability to rapidly measure multiple tactile information simultaneously during brief contact, similar to human touch. We propose a visuotactile sensor guided by contact models, through our investigation of Hertzian contact and planar contact. Specifically, the contact model has revealed the relationship between contact force, depth, area, and the hardness of the contacting objects under contact objects of varying shapes. By embedding these physical priors into a fitting framework, our method avoids data-intensive learning, enabling real-time, simultaneous estimation of 3-axis force, deformation depth, and Shore A hardness. For three tests on the same object, the average error in normal force is around 1.3 N, and the root-mean-square error in hardness is 7.656 on the Shore A scale. At the same time, we have enhanced the material and processing methods of the visuotactile sensor's functional layer to improve its stability and durability, so that it can be adapted to objects of various hardness.**

***Index Terms*—Hardness measurement, simultaneously sensing, visuotactile sensor.**

Received 3 March 2025; revised 18 November 2025; accepted 5 February 2026. Date of publication 23 February 2026; date of current version 6 March 2026. This work was supported in part by the National Key Research and Development Program of China under Grant 2025YFE0113300, in part by the Key Research and Development Program of Zhejiang under Grant 2026SDXT001(SD2), in part by the National Natural Science Foundation of China under Grant 62303407 and Grant T2293720/T2293724, in part by the State Key Laboratory of Industrial Control Technology under Grant ICT2025A08, in part by the State Key Laboratory of Electrical Insulation and Power Equipment under Grant EIPE24212, and in part by the Xiaomi Foundation. The Associate Editor coordinating the review process was Dr. Ernst Csencsics. *(Corresponding authors: Haojian Lu; Xiazhen Yu; Yue Wang.)*

Xiangyu Mi, Ke Qiu, Pingyu Xiang, Rong Xiong, Yue Wang, and Haojian Lu are with the State Key Laboratory of Industrial Control and Technology, Institute of Cyber-Systems and Control, Zhejiang University, Hangzhou 310058, China (e-mail: Xiangyu_Mi@zju.edu.cn; ke.qiu@zju.edu.cn; xiang_py@zju.edu.cn; rxiong@zju.edu.cn; wangyue@iipc.zju.edu.cn; luhaojian@zju.edu.cn).

Shudong Wang is with the State Key Laboratory of Electrical Insulation and Power Equipment, School of Electrical Engineering, Xi'an Jiaotong University, Xi'an 710049, China (e-mail: Shudong_wang@xjtu.edu.cn).

Xiazhen Yu is with the Department of Hepatobiliary and Pancreatic Surgery, The First Affiliated Hospital, Zhejiang University School of Medicine, Hangzhou 310058, China (e-mail: 2314040@zju.edu.cn).

Digital Object Identifier 10.1109/TIM.2026.3667306

I. Introduction

TACTILE sensing is one of the primary modalities used by humans in coordinated interactions [1], [2]. Research has shown that tactile perception is superior to vision and hearing in processing material features and detailed shapes of objects [3], [4], [5]. In addition, the human sense of touch is an irreplaceable and important sense that can simultaneously perceive a variety of physical information, including force, hardness, and temperature, when in contact with an object. To give robots the same or even superior tactile ability as humans, researchers have developed a large number of tactile sensors with different principles. Among them, visuotactile sensors have become an important choice for robot fingertip sensors in recent years due to their high resolution, multimodal sensing, and simple structure.

The visuotactile sensors represented by the GelSight series realize high-precision 3-D reconstruction of contact surfaces based on the photometric stereo method. Multiaxis force estimation and sliding detection are also achieved by adding markers to the gel [6], [7], [8]. However, such sensors require complex optical path arrangements and are computationally intensive for multimodal sensing, making it difficult to measure multiple physical quantities simultaneously. Sensors such as GelStereo and DelTact supplement the missing Z-axis information of monocular vision with binocular stereo vision or randomized pixel dots, sacrificing reconstruction accuracy for faster operation, simpler light arrangement, and the potential of simultaneous measurement [9], [10], [11].

Although tactile sensors have been able to measure physical information such as depth, force, and temperature and can realize dynamic sensing such as slide detection and proximity sensing, there is less research on measuring the hardness of objects. Kimoto and Matsue [12] used piezoelectric ceramic transducers and a parallel plate condenser to measure the hardness with four grades. However, the sensor can only measure a narrow range of hardness, and experiments on objects of different shapes were not performed. Yuan et al. [13] used Gelsight to measure the deformation of the gel's surface and proposed a hardness estimation model with the combination of the brightness function, marker displacement, and normal force field. They also proposed the methods with machine learning [14]. The LSTM and CNN were used in this work, and hardness ranging from 8 to 87 on the Shore 00 scale can be measured with different shapes through a relatively loose operating method. Di et al. [15] took advantage of fiber-optic bundles to miniaturize the visuotactile sensor named DIGIT Pinki. Under conditions of Hertzian contact, they found that the radius of contact is proportional to the cube root of the positive pressure, which can be used to train the network to predict the hardness of the object. Prediction results on spherical silicone hardness samples show that the sensor differentiates hardness from 0.5 to 45 on the Shore A scale. Although these methods offer greater flexibility and more information than traditional sensors, they still face limitations, such as being restricted to objects with specific shapes and exhibiting low accuracy when applied to objects outside the training dataset. The introduction of deep learning also makes the algorithm time-consuming and can only accomplish the measurement of one tactile property at a time.

Considering the problems mentioned above, we propose a stable and durable visuotactile sensor coupled with an algorithm for rapid acquisition of tactile information based on elasticity theory. Our approach enables depth and 3-axis force measurement while simultaneously performing hardness assessment, all while maintaining shape invariance. The contributions of this study are as follows.

1) We propose a stable and durable functional layer for the visuotactile sensors based on optical flow, fabricated by a simple and cost-effective process.
2) A contact model-guided visuotactile sensor is proposed. Our model distinguishes between Hertzian contact and planar contact, revealing the relationship between contact force, depth, area, and the hardness of the contacting objects. Through data fitting based on the physical priors, we have achieved simultaneous measurement of the 3-axis force, deformation depth, and Shore A hardness of the contact object.

II. Hardware Design

A. Selection of the Framework

The support frame is 3-D printed in white photosensitive resin, as shown in Fig. 1(a). To reduce the cost of the visuotactile sensor and simplify the design of the optical path, we use a combination of a monocular camera and a monochromatic light source. The white light is diffusely reflected in the cylindrical cavity to create a uniform and stable light field. LED strips are wrapped around the sensor with a soft strip, and the light source distance can be adjusted as needed.

The functional layer consists of a reflective layer and a protective layer. For the design of the reflective layer, we replaced the random pixel dots used in previous optical flow-based visuotactile sensors with tricolor glitters, while the protective layer uses silver gel instead of spray paint [6], [16].

B. Manufacture of the Function Layer

Water transferring or ink printing is often used to create coatings on gels to measure forces. However, this method can easily result in missing patterns that affect the performance

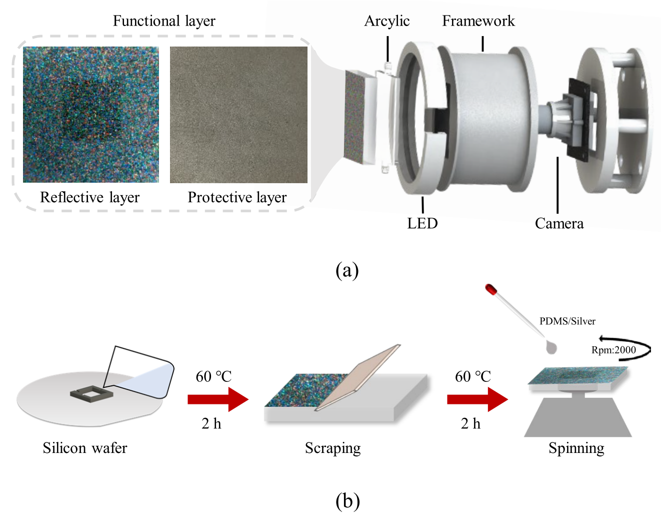

Fig. 1. Schematic of the fast visuotactile sensor. (a) Detailed components of the hardware. (b) Materials for functional layers and fabrication process.

of the sensor. The protective layer of the sensor is typically deposited with a layer of silver metal, and then an additional layer of protective gel is cured on top. An ion sputtering machine is required to deposit the uniform metal, leading to increased fabrication time and cost. In addition, the deposited metal can easily shift or fall off after repeated contact and pressing, rendering the sensor's functional layer ineffective. To solve this problem, we adopted an integrated reflection-protection layer fabrication process, as shown in Fig. 1(b). We fixed the mold on a single-crystal silicon wafer to improve the surface flatness of the contact surface. A polydimethylsiloxane(PDMS)/curing agent mixture with a mass ratio of 10:0.4 is poured into the mold. After 60 °C vacuum curing for 2 h, PDMS mixed with red, green, and blue color glitters is uniformly scraped onto the surface, and the vacuum curing step is repeated. Finally, A 200-μm nanosilver paste-PDMS film is cured on the transparent gel by spin-coating to protect the reflective layer. We used the same material for the entire functional layer, increasing the consistency of the sensor gel deformation. At the same time, its stability has been improved. The proof of the improvement will be given in Section V.

III. Contact Model-Guided Tactile Measurement Method

A. Contact Model

To achieve simultaneous measurement, we need to model the sensor–object contact to simplify the computation. In this article, the sensor operating situation can be divided into two cases: Hertzian contact and planar contact. The Hertzian contact theory describes the elastic contact behavior between two curved bodies (or a curved body and a plane) under load. It provides analytical solutions for key contact parameters such as contact radius r, indentation depth d, and normal force F_n, based on material properties and geometry. The left part of Fig. 2(a) illustrates the classical Hertzian contact between a curved indenter and a curved elastic body. In our case, since

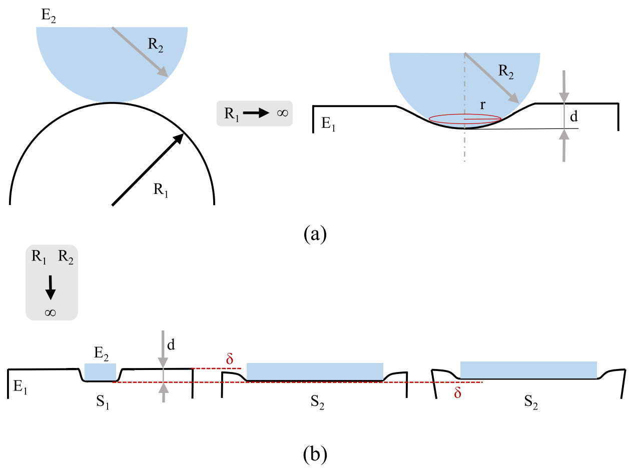

Fig. 2. Illustration of different contact situations. (a) Model of the Hertzian contact. (b) Model of the planar contact.

the gel is fabricated with a planar surface, the radius of curvature of the gel can be taken as $R_1 \to \infty$, which is illustrated on the right part of Fig. 2(a). Under the assumption of small deformation, the Hertzian contact theory yields the relationship as follows [17]:

$$F_n = \frac{4E^* rd}{3} \tag{1}$$

where E^* is the combined Young's modulus, which can be expressed as

$$\frac{1}{E^*} = \frac{1-\nu_1^2}{E_1} + \frac{1-\nu_2^2}{E_2}. \tag{2}$$

In the above equation, E_1 and ν_1 denote Young's modulus and Poisson's ratio of the sensor gel, respectively, while E_2 and ν_2 refer to the same parameters for the contacting object. The effective modulus E^* considers the elastic contributions from both contacting materials and the sensor gel. In our case, E_2 is usually significantly greater than E_1. As a result, the term $(1-\nu_2^2/E_2)$ becomes negligible compared to $(1-\nu_1^2/E_1)$. Thus, the effective modulus can be approximated as

$$\frac{1}{E^*} \approx \frac{1-\nu_1^2}{E_1}. \tag{3}$$

When the radius of curvature of the contacting object $R_1 \to \infty$, it becomes the planar contact in Fig. 2(b). In this circumstance, the deformation of the gel can be solved by approximating the press as a load distribution in the plane [17]

$$d = \frac{F_n\left(1-\nu_1^2\right)}{2rE_1}. \tag{4}$$

Equations (1) and (4) show that for different contact models, the sensor should use different calculations to measure tactile information even under ideal conditions. The method of mixing two models to reduce measurement error also needs to be used with caution. However, the functional layers of visuotactile sensors are generally nonlinear elastic materials, so E_1 varies with the deformation of pressing, and it is still not possible to solve for the analytical solution directly. Nevertheless, during sensor calibration, these equations reveal that the normal force F_n is functionally related to the contact area and indentation depth. By employing the calibration methods proposed in Section III-C, the effects of variations in E_1 can be eliminated.

B. Depth Measurement

It is necessary to distinguish between two concepts: the depth of pressing and the depth of gel deformation. As shown in Fig. 2(b), if the contact area like S_1 is far smaller than the area of gel, the deformation depth of the gel is equal to the pressing depth of the indenter because the pressure acting on a small portion of the deformable material at a neighboring contact will cause only localized stresses that produce localized deformation, which is proved by St. Venant's principle and the law of conservation of energy [17], [18]. However, if the contact area, like S_2, is large, for both compressible and incompressible elastic materials, the deformation depth of the elastic gel will be less than the pressing depth. The difference between the depth of pressing and gel deformation is δ. This is because a uniform pressure perpendicular to the plane of the gel causes an overall displacement of the gel in compressible materials and a lateral expansion of the gel in incompressible materials. For visuotactile sensors, most of the gels, including this article, can be regarded as incompressible materials. Therefore, the smaller the area of the indenter during pressing, the closer the depth of pressing will be to the depth of gel deformation.

The above analysis shows that, taking the average value of the compression depth collected under different areas as the real value to fit the gel deformation depth will rather increase the error of depth measurement. Thus, a standard indenter with a small area and a high degree of rigidity was created for the calibration of the sensor's pressing depth. Details of the calibration process will be given in Section IV-B.

C. 3-Axis Force

Force measurement based on the optical flow field is generally done by the natural-Helmholtz decomposition [19], [20], [21], which means optical flow $\mathbf{f}$ can be decomposed into

$$\mathbf{f} = \mathbf{d} + \mathbf{r} + \mathbf{h} \tag{5}$$

where $\mathbf{d}, \mathbf{r}, \mathbf{h} \in \mathbb{R}^{n\times n\times 2}$ denotes the curl-free field, the divergence-free field, and the harmonic field, respectively. The decomposition of the original optical flow field and the solution of relevant vector equations yield the variables S_n, S_t, and S_τ related to the normal force F_n, tangential force F_t, and in-plane moment F_τ, respectively.

However, the relationship between the normal force F_n and the Helmholtz decomposition S_n is strongly influenced by the area. This is because, as we analyzed in Section III-A, gels are nonlinear elastic objects. The optical flow is greatly affected by the shape of the indenter, and so is the Helmholtz quantity S_n. Moreover, the relationship between F_n and the Helmholtz quantity S_n does not clearly correlate with area. In addition, the use of the Helmholtz decomposition to calculate S_n and S_τ involves a large number of calculations concerning the vector field, which can lead to an increase in the algorithm's time complexity. After using this force estimation algorithm, the frequency of the sensor decreases from 30 to 5 Hz.

So, we go back to the theory of elasticity and combine it with quantitative analysis. In a semi-infinite plane, the normal force F_n can be calculated from the following equation:

$$F_n = m\frac{Erd}{1-\nu^2} = \lambda\frac{E\sqrt{S}d}{1-\nu^2} \tag{6}$$

where S is the contact area and m and $\lambda = (m/\sqrt{\pi})$ are both the size factor. The equation shows that model-based $S_n^m = \sqrt{S}d$ should be an indicator of the normal force F_n. The effects of λ and Young's modulus E can be quantified via calibration using compression tests on indenters of identical hardness but varying contact areas.

As for the shear force F_t, we compute S_t according to (7), since S_t is computed based on the initial optical flow field and no additional matrix calculations are performed [20]

$$S_t = \left|\sum_{i=0,\vec{f_i}\in\mathbf{f}}^{N-1} \vec{f_i}\right|. \tag{7}$$

Theoretically, in-plane moments F_τ generated by a distributed tangential force over a contact area A in the xy plane can be calculated from

$$F_\tau = \int\int_A \left(xf_y - yf_x\right)\, dA \tag{8}$$

where f_x and f_y are the components of the tangential force. When there is a tangential force in the plane, there are only two cases to make the moment zero: the tangential force on the surface is symmetrically distributed in a certain direction, or in a circular contact surface, and all the tangential force directions are radially distributed. However, in practice, perfectly radial and symmetric distributions of tangential force over the contact surface are rare, due to geometric imperfections, surface roughness, and nonuniform loading. Therefore, any significant tangential force is potentially associated with a nonzero torque around the z-axis. Through the simplification, we approximate F_τ as $F_\tau \approx k_\tau \cdot S_t$, where k_τ can be estimated through data fitting, and the very time-consuming Helmholtz decomposition algorithm can be avoided. These equations hold for both Hertzian and planar contacts, but the change in the contact area during Hertzian contact would make the area factor λ not a constant, leading to computational difficulties. Therefore, we only collected data from planar indenters with different areas when performing force fitting.

D. Shape-Independent Hardness Measurement Strategy

Hardness measurement is a complex task, not only because of the various classifications of hardness (Shore, Mohs, etc.) but also because the hardness value is affected by the contact area, the depth of contact, and the contact force [22], [23]. Inspired by the definition of contact hardness, in the task of hardness measurement for visuotactile sensors, we have [24], [25]

$$P = \frac{F_n}{S_{ec}} \tag{9}$$

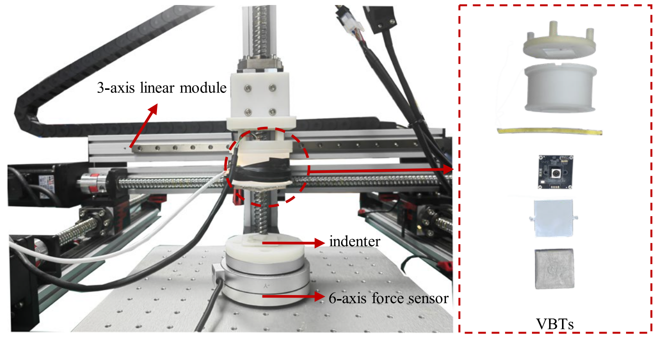

Fig. 3. Sensor data acquisition platform and the details of our visuotactile sensor.

where S_{ec} is the effective contact area. Its physical meaning is the ability of a contacting object to generate force on the sensor gel per unit area and thus can be used as an indicator for hardness. It is worth mentioning that although P is defined as the fraction of force and area, treating it as pressure is wrong because S_{ec} is the effective area due to the skin-in and pile-up [26]. As the depth of press increases, F_n increases rapidly, while the effective contact area hardly changes under planar contact and increases slowly under Hertzian contact. Therefore, P is a function of pressing depth instead of a constant, and it is not the same in planar contact as in Hertzian contact. After plotting the measured values against the depth of gel deformation under planar contact, we observed a linear relationship between these two variables. Thus, we derived an expression for contact hardness with respect to the depth of gel deformation, yielding

$$H_m = \frac{\partial P}{\partial d}. \tag{10}$$

H_m is the Shore A hardness measurement factor, which should be related to the hardness and has shape invariance. Section IV-D will demonstrate that using our proposed hardness factor H_m to predict hardness is more accurate than using other quantities alone.

IV. Implementation Method and Sensor Calibration

A. Experimental Setup

To accurately implement our method and calibrate our sensor, we use a linear motor-driven three-axis slide table for data acquisition, as shown in Fig. 3. The equipment was purchased from Fortune Technology, model FSK40XYZ-L. The repeatability of the three-axis slide is ±0.05 mm with an uncertainty of 0.05 (the above data is based on scale calibration by the manufacturer), and the x- and y-axes are only used to move the sensors to the specified position in the xy plane. Therefore, they are not involved in the calculation of the error and uncertainty. The six-axis force and torque sensor (M4313M2R) purchased from Sunrise Instrument was fixed to an aluminum plate in the xy plane directly below the slide. The full scale range (FSR) of the sensor force and torque is 100 N and 8 N·m, respectively. Its accuracy is represented by three parameters: nonlinearity less than 0.5% FSR, hysteresis

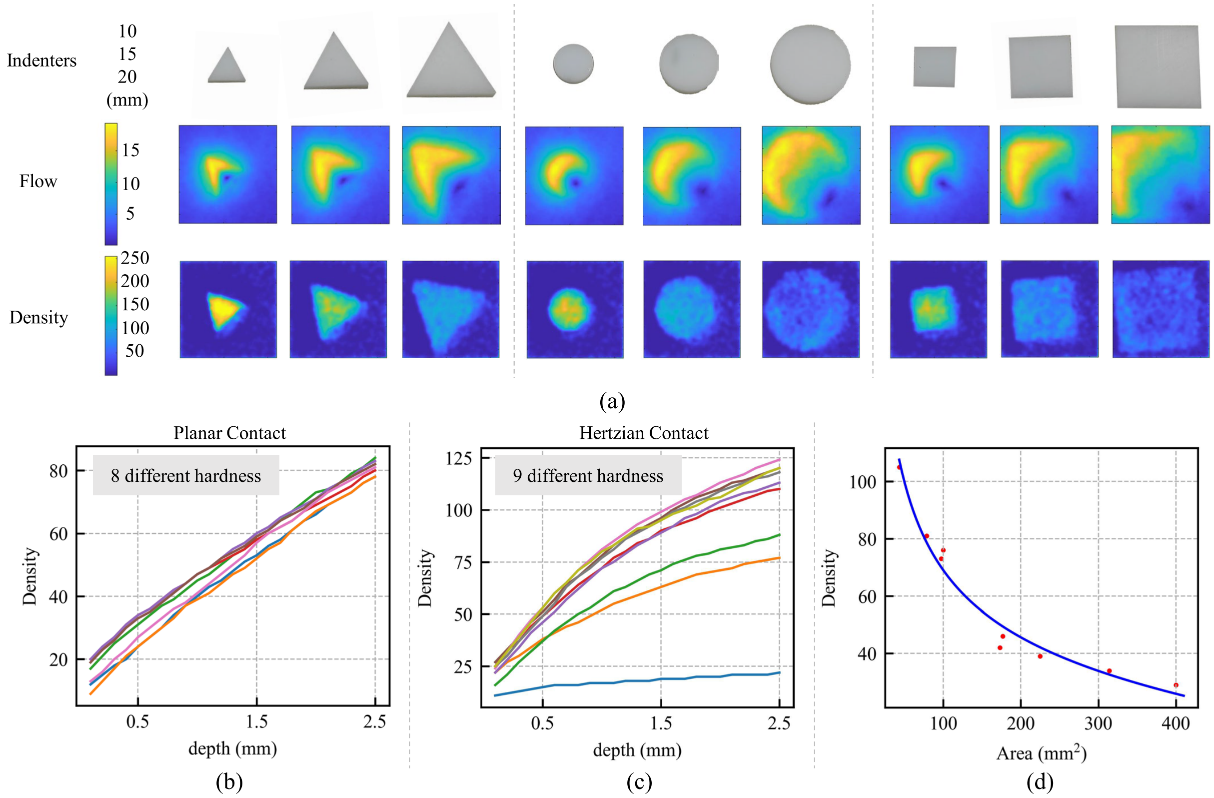

Fig. 4. Methods of depth measurement based on Gaussian density estimation. (a) Indenters with different shapes and areas for depth measurement with related optical flow and Gaussian density. (b) Relationship between depth and density in planar contact. (c) Relationship between depth and density in Hertzian contact. (d) Relationship between area and density in Hertzian contact.

less than 0.5% FSR, and crosstalk less than 2% FSR. The resolution of the force for each channel is 0.033 N, and the resolution of the torque for each channel is 0.003 N·m, with an uncertainty of 0.2% of the measured value. The camera used for the visuotactile sensor is a common monocular camera module with 8 million pixels, and the camera was aberration-corrected before the experiment using the monocular camera calibration function in the MATLAB toolbox. The visuotactile sensor was fixed to the z-end of the slide via an adapter flange. The indenters were affixed to the adapter flange, which is fixedly connected to the force transducer.

All calibration indenters used in this article were fabricated via 3-D printing and include four shapes: triangular, circular, and square flat indenters, as well as hemispherical curved indenters. Each shape was produced in three different sizes: 10, 15, and 20 mm. For circular and hemispherical indenters, the size refers to the diameter, while for triangular and square indenters, it refers to the side length. Each size and shape was further produced with seven different Shore A hardness levels, ranging from 30 to 90 in increments of 10. Since 3-D printing receives a large error due to the influence of materials and processes, all indenters are recalibrated using a Shore A hardness tester before subsequent experiments.

The sensor data acquisition process is as follows. After the z-axis reaches the specified position in the xy plane, it moves downward at a speed of 10 mm/s. When the z-axis force of the 6-axis force transducer is greater than 0.09 N, the system determines that contact occurs and lifts the braking distance upward to make sure that the plane of the visuotactile sensor is just in contact with the indenter without generating force and deformation. Then, the z-axis continues to move downward at a speed of 1 mm/s, and for every 0.1 mm, the visuotactile sensor and the force sensor record the data at the same time until it moves downward by 2.5 mm. The hardness of the indenter for each press is recorded manually after recalibration.

B. Depth Measurement

To demonstrate our theory, we performed Gaussian density tests using indenters shown in the first line of Fig. 4(a). These dimensions are as described in Section IV-A. The relationship between the Gaussian density and depth should both be linear if there is no difference between Hertzian and planar contacts [16]. The second and third lines in Fig. 4(a) show the optical flow and 2-D Gaussian density distributions, respectively, based on the indenter with a hardness of 85, and the compression depth is 2.5 mm. Fig. 4(c) and (d) presents the relationship between depth and Gaussian density under planar and Hertzian contact, respectively. Different colors of the lines indicate different hardness of the indenters. We can see that the Gaussian density is linear with depth only in planar contact because the contact area is a constant in planar contact, but changes in Hertzian contact. As shown in Fig. 4(d), it can be found that at the same pressing depth, different areas of the indenters have a huge effect on the depth of gel deformation, and the maximum Gaussian density tends

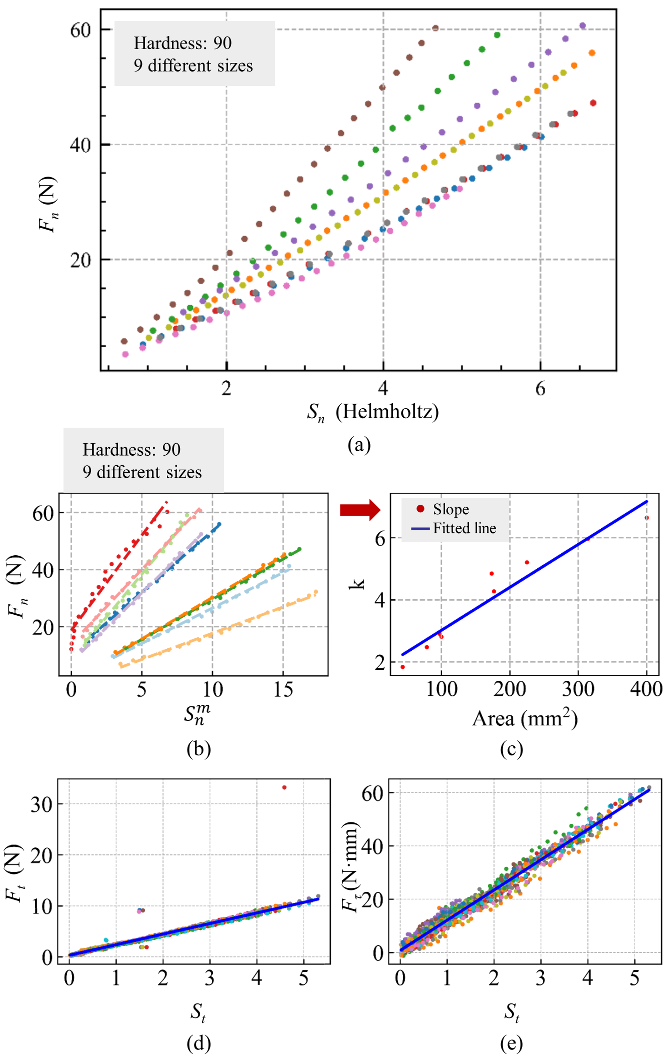

Fig. 5. Methods of 3-axis force measurement based on the contact model. (a) Relationship between normal force and Helmholtz decomposition quantities S_n. (b) Relationship between F_n and S_n^m in different shapes. (c) Relationship between the slope of each line and its contact area in (a). (d) Relationship between F_t and S_t. (e) Relationship between F_τ and S_t.

to decrease rapidly with the increase of the area. Therefore, we no longer use the average value of compressing depth of several indenters with different areas as the ground truth, but use a circle indenter with 98 hardness and 10-mm diameter as the nominal indenter. The gel deformation depth is linearly related to the Gaussian density value in the case of planar contact, with the degree of linearity R^2 reaching 99.25. Therefore, a linear fit is performed between the Gaussian density and the actual deformation depth.

C. 3-Axis Force

Fig. 5(a) shows the true values of F_n versus S_n obtained from our visuotactile sensor for all shapes of the indenter with a hardness of 90. Different colors indicate different contact areas of indenters. It can be seen that the value of S_n varies greatly depending on the area at the same force. It proves our theory presented in Section III. Fig. 5(b) shows the proposed parameter S_n^m versus F_n under exactly the same conditions.

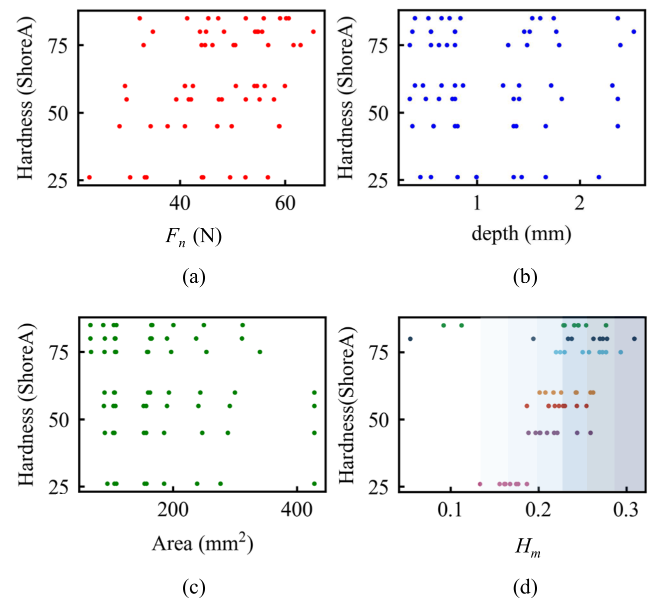

Fig. 6. Analysis of influencing factors related to hardness measurements. (a) Relationship between hardness and normal force. (b) Relationship between hardness and gel deformation depth. (c) Relationship between hardness and contact area. (d) Relationship between hardness and proposed hardness indicator H_m.

During the change of pressing from 0 to 2.5 mm with the same indenter, F_n and S_n^m show a nearly linear relationship. Moreover, the slope of the pressing curve varies for different sizes of indenters due to the variation of λ and E, as shown in Fig. 5(c). Thus, we plot the slope k of the loading curve versus the contact area for different indenters, and find that k also shows a nearly linear relationship with the contact area. This implies that we can set an area excitation to boost the force of those areas that are too large. The relationship between F_t and S_t as well as F_τ and S_t is shown in Fig. 5(d) and (e), respectively. We can find that the relationships are not affected by the contact area. Finally, the 3-axis force $\mathbf{F} = [F_n, F_t, F_\tau]^T$ can be obtained by fitting the above three variables with linear regression or a multilayer perceptron (MLP)

$$\mathbf{F} = \mathbf{\Gamma} \cdot \left[g(A) \cdot S_n, S_t, S_t\right]^T \tag{11}$$

where $g(A)$ is the incentive function calculated in Fig. 5(b), which is related to the contact area A. $\mathbf{\Gamma}$ is the fitting function vector, $[\gamma_1(x), \gamma_2(x), \gamma_3(x)]$.

D. Shape-Independent Hardness Measurement

From Fig. 6(a)–(c), we can find that using any single factor of depth, area, or force does not predict hardness. In contrast, Fig. 6(d) shows that H_m is much more correlated with hardness than the other three factors, although it does not completely eliminate the effect from the area. This is because we take the cut-line modulus to approximate Young's modulus, treating it as a linear elastomer. Nevertheless, our method can still measure an object's hardness within an error.

We use linear regression to predict the hardness of planar contact based on H_m. In addition, as mentioned in the above

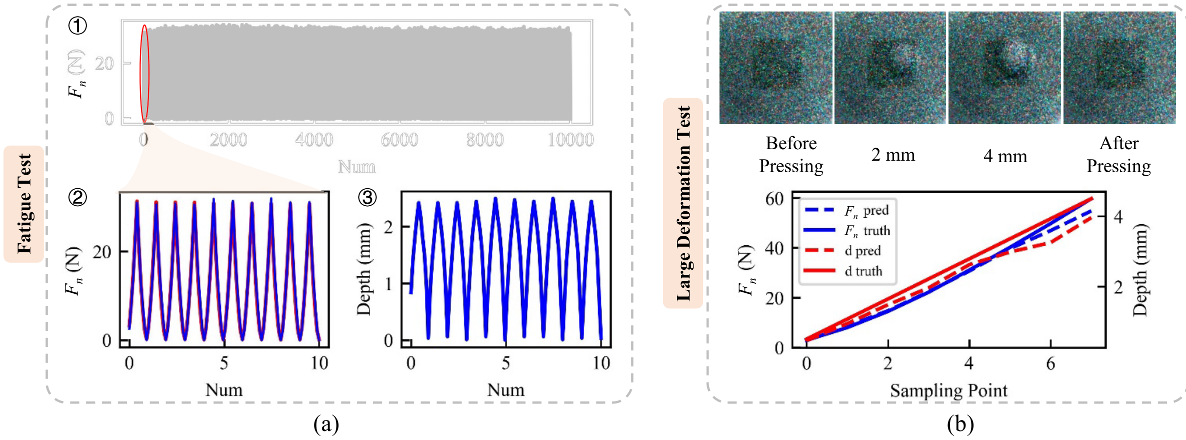

Fig. 7. Experiments for the proposed stable and durable functional layer. (a) Normal force and depth tracking during ten thousand presses. (b) Normal force and depth tracking during the large deformation press.

analysis, the relationship between H_m and Shore A hardness in Hertzian contact is different from that in planar contact, and it is necessary to calculate the two separately in hardness measurement. Considering the complex relationship between force, area, and depth during Hertzian contact, we use a multilayer perceptron to predict the hardness of Hertzian contact. It contains an input layer, a hidden layer with ten neural units, and an output layer. For the hardness measurement, we only need to preinput the contact model, which can be achieved by adding an additional camera.

TABLE I
RMSE OF FORCES FOR DIFFERENT INDENTERS

	$F_n(N)$	$F_t(N)$	$F_\tau(N \cdot m)$
Triangle	1.080	1.326	0.076
Circle	1.470	1.882	0.132
Rectangle	1.662	1.234	0.118
Hemisphere	1.574	0.498	0.041

V. EXPERIMENTS AND RESULTS

A. Durability and Stability

To prove the proposed functional layer's stability and durability, we first conducted a 10 000-cycle compression fatigue test, during which the normal force and depth output from the visuotactile sensor are continuously recorded and compared with the true value. As shown in the first figure of Fig. 7(a), the peak force measured by the sensor stays within a stable range during the test. Comparing the force measurement curves from the first ten presses with the true value as shown in the second picture of Fig. 7(a), we can see that the sensor measures (blue line) and tracks the true contact force (red line) very well. In addition, the press depth output from the sensor is consistently close to the true value. After that, we complete the sensor gel limit pressing test. Since the total thickness of the functional layer of our sensor is 5 mm, we control the three-axis table to press down a depth of 4 mm, concerning the safe operation of the instrumentation. As shown in Fig. 7(b), the gel does not show any breakage and shape change before and after the extreme pressing test, and the sensor still outputs the depth of gel deformation and contact force normally during the test, but when the depth is greater than 2.5 mm, the measured normal force has a large error with the real value.

B. Measurement of Hardness and Tactile Information

The results of simultaneous measurement of tactile information are shown in Fig. 8. We have realized the 3-D reconstruction of the indenter surface based on the sensor-measured depth map, as shown in Fig. 8(a). For various shapes of the indenter with different contact models, our proposed method can more accurately restore the real situation of the gel deformation. The resolution of depth can reach 0.1 mm. The standard uncertainty of depth measurement, evaluated from multiple repetitions of indentation by the smallest and hardest triangular indenter, is determined to be 0.2 mm. Fig. 8(b) proves the difference between the depth of indenter pressing and the depth of gel deformation during pressing, and the larger the contact area, the larger the difference between the two.

Fig. 8(c) shows the measurement and tracking of the 3-axis force of a triangular indenter with a side length of 10 mm and a hardness of 40 during a 2.5-mm press test, demonstrating the accuracy and tracking performance of force measurement. Fig. 8(d) and (e) shows the normal force of nine hemispherical indenters with different hardnesses and nine flat indenters with different shapes during pressing, respectively. The results indicate that the sensor can measure the pressing normal force accurately except for the indenter with a hardness of 5. The resolution of force and torque is 0.5 N and 0.1 N·m, respectively. The measurement errors for different indenters are shown in Table I, which is also the uncertainty of force and torque measurement. Considering that the proposed visuotactile sensor can measure forces up to 70 N, these errors are within acceptable limits. Using our proposed hardness measurement factor, the hardness of

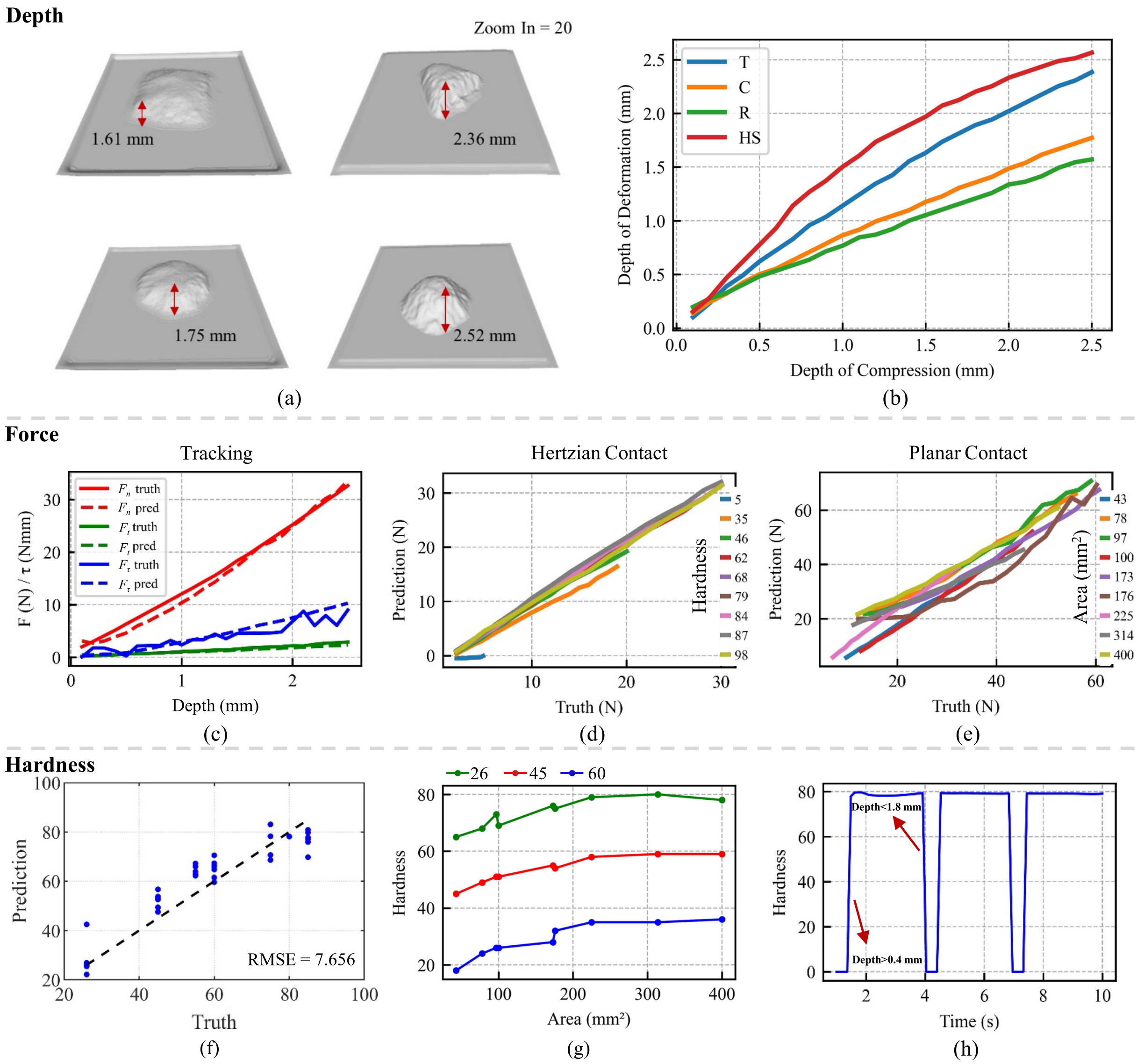

Fig. 8. Results of simultaneous measurement of tactile information. (a) Reconstruction of indenters through the depth map. (b) Depth of gel deformation measured by the visuotactile sensor is different from the depth of compression. (c) 3-axis force tracking during contact. (d) Prediction of normal force under Hertzian contact. (e) Prediction of normal force under planar contact. (f) Prediction of hardness for all indenters. (g) Hardness measurement for indenters with different sizes. (h) Hardness measurement during pressing.

objects with different areas and shapes can be measured more accurately within the Shore A hardness range of 20–80, as shown in Fig. 8(f). It also shows that the resolution of hardness is 5, and the uncertainty is around 8 based on the root-mean-square error obtained from the test dataset. The accuracy of measurements decreases for hardness values above 80. However, objects with hardness values exceeding 80 are less likely to be damaged during actual grasping, making our method particularly suitable for soft object manipulation using dexterous robotic hands. In addition, Fig. 8(g) shows the variation of hardness measurements when the sensor is pressed by indenters of different areas but the same hardness value (26, 45, and 60). Although we have not completely eliminated the effect of size on hardness measurements, the sensor can measure objects with different shapes to an approximate range that is sufficient to differentiate between hardnesses at various levels. From Fig. 8(h), we can also find that as long as the pressing depth is greater than the sensor's minimum response depth of 0.4 mm and less than 1.8 mm, that is, the deformation of the sensor gel is kept within a small deformation range, the sensor can output a stable hardness value.

In addition, to better demonstrate the versatility of our approach, we collect data from seven objects with different materials, shapes, and hardness levels. Each object is calibrated using a Shore A hardness tester, and none of these objects are included in our training set. As shown in Fig. 9, our method successfully distinguishes the hardness of cylindrical indenters made from different materials. Even when the indenters are of the same size and material but have different contact models, our sensor still achieves accurate measurements. The error bars in the figure also reflect the uncertainty in the measurement of the object's hardness.

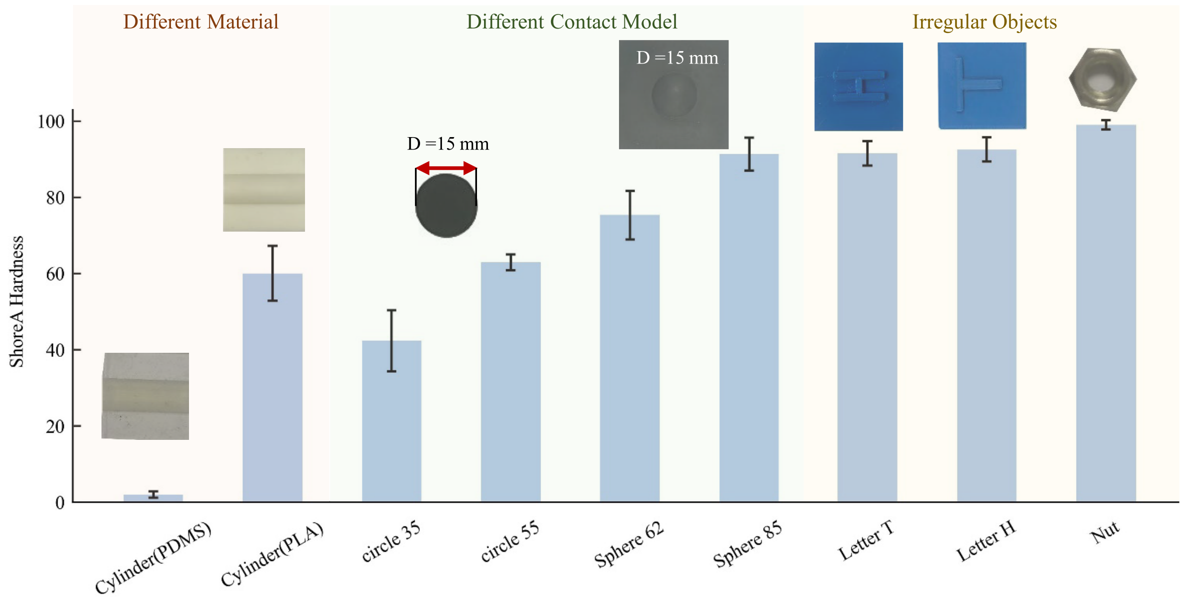

Fig. 9. Hardness measurement for a wide range of objects.

Moreover, we tested the hardness of irregularly shaped indenters, including those shaped like "H" and "T," as well as a nut. These tests validate the robustness and versatility of our approach in handling objects of diverse geometries. Although the sensor can still differentiate between hard and soft objects, it fails to provide accurate hardness values. This issue is particularly evident when testing everyday objects such as nuts. The measured hardness values can vary significantly when tested from different angles. The reason is that the contact surfaces on the edges of the nut are extremely small and can be considered discontinuous. As a result, our contact model becomes inapplicable in such scenarios.

VI. Conclusion and Future Work

In this article, we propose a visuotactile sensor that incorporates a new functional layer material, significantly improving the durability and load capacity of the sensor. This makes it more suitable for long-term use in robotic applications. In addition, based on the elasticity theory, we propose the contact model of the visuotactile sensor gel with the objects and propose a contact depth measuring method guided by modeling, so that the depth estimation will hardly be affected by the area of the object. Building on this foundation, we also present a new 3-axis force and a hardness measurement method independent of the shape. All tactile information can be measured simultaneously in the short time that contact occurs. We believe that this work can facilitate the practical application of visuotactile sensors in robotic dexterous hands. In the future, we will reduce the size of the sensor and further optimize the accuracy of the sensor so that it can be fully adapted to the feedback grasping task of dexterous hands.

References

[1] Q. Li, O. Kroemer, Z. Su, F. F. Veiga, M. Kaboli, and H. J. Ritter, "A review of tactile information: Perception and action through touch," *IEEE Trans. Robot.*, vol. 36, no. 6, pp. 1619–1634, Dec. 2020.

[2] R. S. Dahiya, G. Metta, M. Valle, and G. Sandini, "Tactile sensing—From humans to humanoids," *IEEE Trans. Robot.*, vol. 26, no. 1, pp. 1–20, Jan. 2009.

[3] S. Luo, J. Bimbo, R. Dahiya, and H. Liu, "Robotic tactile perception of object properties: A review," *Mechatronics*, vol. 48, pp. 54–67, Dec. 2017.

[4] R. S. Dahiya and M. Valle, *Robotic Tactile Sensing: Technologies and System*, vol. 1. Cham, Switzerland: Springer, 2013.

[5] S. Lederman and R. Klatzky, "Tutorial review haptic perception: A tutorial," *Attention, Perception Psychophysics*, vol. 71, no. 7, pp. 1439–1459, 1983.

[6] W. Yuan, S. Dong, and E. Adelson, "GelSight: High-resolution robot tactile sensors for estimating geometry and force," *Sensors*, vol. 17, no. 12, p. 2762, Nov. 2017.

[7] S. Wang, Y. She, B. Romero, and E. Adelson, "Gelsight wedge: Measuring high-resolution 3D contact geometry with a compact robot finger," in *Proc. IEEE Int. Conf. Robot. Autom. (ICRA)*, May 2021, pp. 6468–6475.

[8] E. Donlon, S. Dong, M. Liu, J. Li, E. Adelson, and A. Rodriguez, "GelSlim: A high-resolution, compact, robust, and calibrated tactile-sensing finger," in *Proc. IEEE/RSJ Int. Conf. Intell. Robots Syst. (IROS)*, Oct. 2018, pp. 1927–1934.

[9] S. Cui, R. Wang, J. Hu, C. Zhang, L. Chen, and S. Wang, "Self-supervised contact geometry learning by GelStereo visuotactile sensing," *IEEE Trans. Instrum. Meas.*, vol. 71, pp. 1–9, 2022.

[10] C. Zhang et al., "GelStereo 2.0: An improved GelStereo sensor with multimedium refractive stereo calibration," *IEEE Trans. Ind. Electron.*, vol. 71, no. 7, pp. 7452–7462, Jul. 2024.

[11] G. Zhang, Y. Du, H. Yu, and M. Y. Wang, "DelTact: A vision-based tactile sensor using a dense color pattern," *IEEE Robot. Autom. Lett.*, vol. 7, no. 4, pp. 10778–10785, Oct. 2022.

[12] A. Kimoto and Y. Matsue, "A new multifunctional tactile sensor for detection of material hardness," *IEEE Trans. Instrum. Meas.*, vol. 60, no. 4, pp. 1334–1339, Apr. 2011.

[13] W. Yuan, M. A. Srinivasan, and E. H. Adelson, "Estimating object hardness with a GelSight touch sensor," in *Proc. IEEE/RSJ Int. Conf. Intell. Robots Syst. (IROS)*, Oct. 2016, pp. 208–215.

[14] W. Yuan, C. Zhu, A. Owens, M. A. Srinivasan, and E. H. Adelson, "Shape-independent hardness estimation using deep learning and a GelSight tactile sensor," in *Proc. IEEE Int. Conf. Robot. Autom. (ICRA)*, May 2017, pp. 951–958.

[15] J. Di et al., "Using fiber optic bundles to miniaturize vision-based tactile sensors," 2024, *arXiv:2403.05500*.

[16] Y. Du, G. Zhang, Y. Zhang, and M. Y. Wang, "High-resolution 3-dimensional contact deformation tracking for FingerVision sensor with dense random color pattern," *IEEE Robot. Autom. Lett.*, vol. 6, no. 2, pp. 2147–2154, Apr. 2021.

[17] A. I. Lurie, *Theory of Elasticity*. Cham, Switzerland: Springer, 2010.

[18] M. Leven, *Photoelasticity: The Selected Scientific Papers of MM Frocht*. Amsterdam, The Netherlands: Elsevier, 2013.

[19] H. Bhatia, V. Pascucci, and P.-T. Bremer, "The natural helmholtz-hodge decomposition for open-boundary flow analysis," *IEEE Trans. Vis. Comput. Graphics*, vol. 20, no. 11, pp. 1566–1578, Nov. 2014.

[20] Y. Zhang, Z. Kan, Y. Yang, Y. A. Tse, and M. Y. Wang, "Effective estimation of contact force and torque for vision-based tactile sensors with Helmholtz–Hodge decomposition," *IEEE Robot. Autom. Lett.*, vol. 4, no. 4, pp. 4094–4101, Oct. 2019.

[21] B. Fang et al., "Force measurement technology of vision-based tactile sensor," *Adv. Intell. Syst.*, vol. 7, no. 1, 2024, Art. no. 2400290.

[22] J. Marteau, M. Bigerelle, Y. Xia, P.-E. Mazeran, and S. Bouvier, "Quantification of first contact detection errors on hardness and indentation size effect measurements," *Tribol. Int.*, vol. 59, pp. 154–162, Mar. 2013.

[23] C. Dhong et al., "Role of indentation depth and contact area on human perception of softness for haptic interfaces," *Sci. Adv.*, vol. 5, no. 8, p. 8845, Aug. 2019.

[24] Y.-T. Cheng and C.-M. Cheng, "What is indentation hardness?," *Surf. Coat. Technol.*, vol. 133, pp. 417–424, Apr. 2000.

[25] E. Holm, R. Holm, and E. I. Shobert, "Theory of hardness and measurements applicable to contact problems," *J. Appl. Phys.*, vol. 20, no. 4, pp. 319–327, Apr. 1949.

[26] E. Broitman, "Indentation hardness measurements at macro-, micro-, and nanoscale: A critical overview," *Tribol. Lett.*, vol. 65, no. 1, p. 23, Mar. 2017.

Xiangyu Mi received the B.E. degree from the School of Mechanical Engineering, Xi'an Jiaotong University, Xi'an, China, in 2022. He is currently pursuing the Ph.D. degree with the College of Control Science and Engineering, Zhejiang University, Hangzhou, China.

His research interests include visuotactile sensors, triboelectric sensors, and the control of robots.

Ke Qiu received the B.E. degree in mechanical engineering with specialization in mechatronics from the School of Mechanical Engineering, Zhejiang University, Hangzhou, China, in 2022, where he is currently pursuing the Ph.D. degree with the College of Control Science and Engineering.

Pingyu Xiang (Graduate Student Member, IEEE) received the B.E. degree in mechatronics engineering from the School of Mechanical Engineering, Zhejiang University, Hangzhou, China, in 2022, where he is currently pursuing the Ph.D. degree in control science and engineering with the College of Control Science and Engineering, under the supervision of Prof. Lu.

His research interests include continuum robotics, medical robotics, and machine learning.

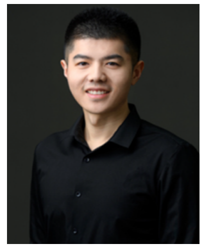

Shudong Wang (Member, IEEE) received the joint Ph.D. degree in instrument science and technology from Xi'an Jiaotong University, Xi'an, China, and the City University of Hong Kong, Hong Kong, SAR, in 2021.

He is currently an Assistant Professor at the School of Electrical Engineering, Xi'an Jiaotong University. His research interests include the design and integration of microelectromechanical sensors.

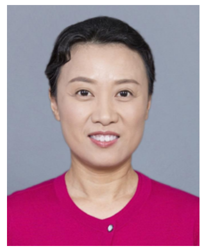

Rong Xiong (Senior Member, IEEE) received the Ph.D. degree in control science and engineering from the Department of Control Science and Engineering, Zhejiang University, Hangzhou, China, in 2009.

She is currently a Professor at the Department of Control Science and Engineering, Zhejiang University. Her latest research interests include motion planning and SLAM.

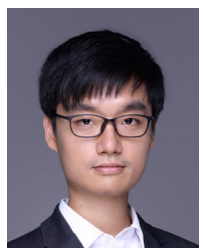

Yue Wang (Senior Member, IEEE) received the Ph.D. degree in control science and engineering from the Department of Control Science and Engineering, Zhejiang University, Hangzhou, China, in 2016.

He is currently a Professor at the Department of Control Science and Engineering, Zhejiang University. His latest research interests include mobile robotics and robot perception.

Xiazhen Yu received the Ph.D. and M.D. degrees in surgery from the Department of School of Medicine, Zhejiang University, Hangzhou, China, in 2014.

He is currently an Associate Chief Physician with the Department of Hepatobiliary and Pancreatic Surgery, The First Affiliated Hospital, Zhejiang University School of Medicine. His latest research interests include liver transplantation and machine learning.

Haojian Lu (Member, IEEE) received the B.Eng. degree in mechatronics engineering from Beijing Institute of Technology, Beijing, China, in 2015, and the Ph.D. degree in robotics from the City University of Hong Kong, Hong Kong, in 2019.

He is currently a Professor at the State Key Laboratory of Industrial Control and Technology and Institute of Cyber-Systems and Control, Zhejiang University, Hangzhou, China. His research interests include micro/nanorobotics, bioinspired robotics, medical robotics, microaerial vehicles, and soft robotics.